High-Throughput MLD for Advanced EUV Photoresists: Stability and Performance of Organic–Inorganic Hybrid Films

Duncan Reece[1], Emily Crum[1], Jane Keth[1], David S. Bergsman[1]

July 16, 2025

Abstract

As extreme ultraviolet (EUV) lithography continues to push toward sub-10 nm semiconductor patterning, next-generation photoresists must meet increasingly stringent demands for resolution, sensitivity, line-edge roughness, and etch durability. Hybrid organic–inorganic thin films, particularly alucones and zincones deposited via molecular layer deposition (MLD), provide precise tunability of chemical structure, uniformity of deposition, and intrinsic plasma etch resistance, making them promising EUV resist candidates. In this study, we systematically evaluate alucone and zincone films synthesized using a series of bifunctional organic diols to elucidate how structure and composition affect lithographic performance. Film deposition parameters were optimized, and films were comprehensively characterized by spectroscopic ellipsometry, Fourier-transform infrared spectroscopy (FTIR), and X-ray photoelectron spectroscopy (XPS). Stability assessments under ambient conditions, solvent immersion, and controlled ultraviolet (UV) irradiation provided detailed insights into dissolution mechanisms and photochemical cross-linking pathways. Electron-beam lithography experiments validated their resist capabilities, demonstrating sub-50 nm resolution and improved lithographic contrast attributed to UV-induced organic cross-linking. These results establish alucone and zincone systems as versatile platforms for EUV photoresist development, presenting a comprehensive structure–property framework to guide the rational design of advanced lithographic materials.

Introduction

Extreme ultraviolet (EUV) lithography at 13.5 nm has emerged as the principal exposure technology for advanced-node logic and memory fabrication, routinely enabling half-pitch dimensions below 20 nm [1, 2]. To fully leverage this capability, photoresist materials must simultaneously achieve high sensitivity $\leq 20\,\text{mJ/cm}^2$, low line-edge roughness (LER $\leq$ 3 nm), precise critical dimension control, and robust plasma etch resistance—criteria that have historically challenged conventional chemically amplified resists (CARs) [3–5].

CAR formulations rely on acid diffusion mechanisms, leading to inherent trade-offs among sensitivity, resolution, and LER, and often fail to deliver sufficient inorganic content for advanced etch processing [6]. Consequently, significant attention has shifted toward alternative resist platforms, particularly metal-rich and hybrid organic–inorganic materials, which promise improved etch resistance, resolution, and radiation sensitivity [7–10].

Early inorganic candidates, including hydrogen silsesquioxane (HSQ) and perhydrogen polysilazane, offered excellent etch durability but required impractically high exposure doses and were prone to swelling during development [8]. More recent approaches utilizing tin-oxo clusters and hafnium oxide nanoparticles have achieved pattern resolutions below 15 nm. However, their reliance on colloidal processes often complicates film uniformity and defectivity control [7, 8].

Hybrid organic–inorganic thin films fabricated via molecular layer deposition (MLD) offer an attractive alternative by combining inorganic durability with tunable organic components, thereby enabling precise control over solubility, cross-link density, and radiation chemistry [11–14]. Due to the inherently self-limiting, surface-controlled nature of MLD reactions, these films achieve exceptional thickness uniformity, compositional precision, and molecular-level tunability—features difficult to replicate with solution-based processing [11, 15, 16].

Alucones and zincones, hybrid networks generally described by the repeating structural units $[\text{Al}-\text{O}-\text{R}-\text{O}]_n$ and $[\text{Zn}-\text{O}-\text{R}-\text{O}]_n$, respectively, where R is a divalent organic linker derived from bifunctional diols, have emerged as model systems for studying hybrid resist behavior [17, 18]. Molecular layer deposition involves sequential exposures to a metal alkyl precursor (trimethylaluminum for alucones, diethylzinc for

zincones) and a bifunctional organic diol ($HO - R - OH$), resulting in a precisely constructed metal–oxygen–carbon hybrid framework. The inorganic M–O backbone (M = Al or Zn) provides mechanical stability and etch resistance, while the organic linker defines free volume, radiation sensitivity, and developer solubility [14, 19].

By employing linkers spanning saturated, unsaturated, and aromatic structures, the stereochemical and electronic influences on resist performance can be systematically investigated. However, evaluating such diverse metal–organic combinations is experimentally intensive, as each system requires independent optimization of precursor dosing, purge timing, and thermal conditions. Traditional single-chamber reactors impose prohibitive time constraints for such combinatorial studies.

To address this limitation, we developed a high-throughput MLD reactor featuring six independent deposition chambers, enabling simultaneous growth of distinct chemistries with undetectable cross-contamination [20]. Using this platform, alucone and zincone films incorporating ethane-1,2-diol (EG), 2-methylene-1,3-propanediol (MPD), 3,4-dihydroxy-1-butene (DHB), cis-2-butene-1,4-diol (CB), 1,4-butynediol (BTY), and 1,3,4-trihydroxybenzene (THB) were systematically synthesized to elucidate the effects of organic linker chemistry on resist properties.

Three critical performance metrics were assessed: (i) air stability via in situ ellipsometry, (ii) developer compatibility across organic solvents and aqueous solutions, and (iii) lithographic performance using electron-beam lithography (EBL). Complementary Fourier-transform infrared spectroscopy (FTIR) and X-ray photoelectron spectroscopy (XPS) analyses were performed to probe chemical transformations such as bond cleavage, cross-linking, and structural reorganization within the hybrid networks.

Collectively, this comprehensive evaluation establishes detailed structure–property correlations linking organic linker chemistry, metal center selection, and lithographic performance. The mechanistic insights derived herein lay the groundwork for rational design of next-generation hybrid EUV photoresists tailored to meet the stringent demands of sub-10 nm semiconductor patterning.

Experimental Methods

Substrate Preparation

Silicon wafers (University Wafers) with a native oxide thickness of approximately $16\,\text{Å}$ were diced into $1.5 \times 1.5\,\text{cm}^2$ squares. Substrates were cleaned using freshly prepared piranha solution (7:3 v/v, $30\,\%$ H_2O_2 in concentrated H_2SO_4) for $15\,\text{min}$, rinsed thoroughly with deionized water, and dried under a flow of nitrogen gas. **Caution:** Piranha solution is highly corrosive and exothermic; appropriate safety precautions were observed. Surface hydroxylation induced by piranha cleaning facilitated subsequent molecular layer deposition (MLD) growth.

Precursors

Inorganic precursors were trimethylaluminum (TMA, $98\,\%$, Strem Chemicals) and diethylzinc (DEZ, $98\,\%$, Strem Chemicals). Organic diols—ethane-1,2-diol (EG), cis-2-butene-1,4-diol (CB), 2-methylene-1,3-propanediol (MPD), 1,3,4-trihydroxybenzene (THB), 1,4-butynediol (BTY), and 3,4-dihydroxy-1-butene (DHB)—were used without further purification. Precursor details including purities and suppliers are summarized in Supplementary Table S1.

Molecular Layer Deposition (MLD)

Hybrid organic–inorganic thin films were deposited using a custom-built six-chamber high-throughput MLD reactor previously described [20]. Depositions were performed at $120\,°\text{C}$. Precursor dosing times, purge intervals, and chamber pressures were individually optimized to achieve self-limiting growth. Typical dosing pressures were approximately $200\,\text{mTorr}$ with purge pressures reduced to $50\,\text{mTorr}$. Deposition parameters for each precursor are provided in Supplementary Table S2. Film thicknesses were controlled by adjusting the number of deposition cycles, typically targeting $20\,\text{nm}$ to $80\,\text{nm}$ thick films (approximately 100 cycles).

Air Stability Measurements

Film thicknesses and optical constants were measured immediately after deposition and after ambient air exposures of 1 h and 24 h at 20 °C and 40 % to 50 % relative humidity. Measurements were conducted using spectroscopic ellipsometry (AlphaSE, J.A. Woollam Co.). Thickness modeling employed either fixed-parameter Cauchy dispersion or generalized oscillator (GenOsc) models. Typical mean square error (MSE) values were approximately 1 for Cauchy-fitted films and less than 5 for GenOsc-fitted thicker films.

UV Irradiation

Samples were irradiated continuously at 254 nm using a 6 W low-pressure mercury lamp (Cole-Parmer) housed in a custom-built enclosure. The irradiance at the sample position was $0.2\,\mathrm{mJ/(cm^2 \cdot s)}$, delivering a cumulative exposure dose of approximately $16\,\mathrm{J/cm^2}$ over 24 h.

Developer Screening

To evaluate chemical robustness, films were immersed for 1 h in anhydrous organic solvents (acetone, toluene, chloroform) under nitrogen atmosphere or aqueous solutions (deionized water, 0.01 M HCl, 0.01 M KOH) under ambient conditions. After immersion, samples were rinsed with isopropanol and dried under nitrogen. Thicknesses and refractive indices were measured post-development. The 1 h immersion was deliberately chosen as an aggressive initial screening to determine conditions capable of fully removing the films. For promising materials, developer contrast curves at reduced immersion times were subsequently generated to estimate suitable development windows.

Electron-Beam Lithography (EBL)

Electron-beam lithography was performed using a JEOL JBX-6300FS system operating at 100 kV and 8 nA. Dose-matrix patterns were exposed using electron doses ranging from $500\,\mathrm{\mu C/cm^2}$ to $5000\,\mathrm{\mu C/cm^2}$. CAD layouts for dose-matrix and box-and-grating patterns were created using LayoutEditor software and processed with BEAMER software (GenISys GmbH) to assign electron doses and prepare JEOL-compatible files. Final pattern designs, including square dose labels and line dimensions, are provided in Sup-

plementary Figure S1.

Development of exposed films was conducted in 0.01 M HCl for exposure times between 5 s and 10 s, followed by rinsing with deionized water and drying under nitrogen.

Film Characterization

Film thicknesses and optical constants were measured by spectroscopic ellipsometry. Surface compositions were analyzed by X-ray photoelectron spectroscopy (XPS, Kratos Axis Ultra DLD). Infrared spectra were collected using a Thermo Scientific Nicolet iS50R Research FTIR Spectrometer equipped with an attenuated total reflectance (ATR) accessory. Surface morphology and patterning quality were examined by scanning electron microscopy (SEM, Thermo Fisher Apreo 1) and atomic force microscopy (AFM, Bruker Dimension FastScan).

Solid-State NMR

Solid-state ^{13}C NMR spectra were recorded using a Bruker AV-700 spectrometer operating at a ^{1}H frequency of 700.38 MHz with a triple-resonance magic-angle spinning (MAS) probe accommodating 3.2 mm rotors. Samples were spun at rates up to 24 kHz. Data were collected using TopSpin 3.7 software, with automatic tuning and matching (ATMA) and variable temperature control between $-80\,°C$ to $120\,°C$.

Results and Discussion

Hybrid Film Growth and Thickness Control

Hybrid organic–inorganic thin films were deposited via molecular layer deposition (MLD) using trimethylaluminum (TMA) or diethylzinc (DEZ) with bifunctional organic diol precursors. Growth per cycle (GPC) values ranged from approximately 1 Å/cycle to 6 Å/cycle, consistent with controlled, stoichiometric MLD growth and avoidance of chemical vapor deposition (CVD)-like behavior [21].

Alucone films (TMA-based) consistently exhibited higher GPCs than zincone films (DEZ-based) across all organic linkers, typically between 3 Å/cycle to 6 Å/cycle. Among these, alucones synthesized with 1,4-butynediol (BTY) achieved the highest GPCs (up

to 6 Å/cycle), attributed to the rigidity and linear geometry imposed by the internal carbon–carbon triple bond. This structural constraint likely enhances monolayer formation by reducing conformational flexibility and improving surface reactivity [22]. Intermediate GPC values were observed for alucones formed from cis-2-butene-1,4-diol (CB), 2-methylene-1,3-propanediol (MPD), and 1,3,5-trihydroxybenzene (THB), reflecting the influence of steric bulk, branching, and aromaticity on saturation behavior.

Zincone films exhibited lower and more variable GPCs (1 Å/cycle to 4 Å/cycle), which may stem from less favorable adsorption dynamics or weaker Zn–O–C bonding [23].[1] However, these values are likely underestimated due to post-deposition hydrolysis and partial film loss prior to ellipsometric measurement. This phenomenon is discussed further in Section **??**.

Final film thicknesses were tuned between 20 nm to 80 nm by varying the number of MLD cycles (typically 100). Spectroscopic ellipsometry confirmed high uniformity and reproducibility across batches (Supplementary Figure S1), validating the MLD process as a robust and scalable platform for subsequent evaluations.

Air Stability and Degradation Resistance

The environmental stability of hybrid films was evaluated by monitoring changes in thickness after ambient air exposure at 20 °C and 40 % to 50 % relative humidity for 1 h and 24 h. Thicknesses were measured by spectroscopic ellipsometry.

Zincone films exhibited rapid and severe degradation, losing over 40% of their thickness within the first 10 min. This pronounced instability is attributed to the hydrolytic vulnerability of Zn–O–C bonds, due to the electrophilicity of zinc centers and the relatively weak coordination compared to aluminum-based analogues [24]. Ultraviolet (UV) exposure at 254 nm modestly slowed degradation rates, but significant thickness loss still occurred over 24 h, especially for films based on ethylene glycol (EG), 2-methylene-1,3-propanediol (MPD), and 3,4-dihydroxy-1-butene (DHB).

In contrast, alucone films demonstrated superior air stability. As-deposited alucones showed moderate thickness reductions (10 % to 20 %) over 24 h, whereas UV-treated alucones retained over 95% of their original thickness. This enhancement is attributed to UV-induced crosslinking and network densification, which reduce moisture access to

---

[1]Citation to be confirmed.

reactive sites [25].

These results underscore the critical role of metal center identity and crosslink density in determining environmental robustness. The strong contrast in degradation behavior between zincones and alucones supports the selection of aluminum-based hybrid networks for further lithographic development.
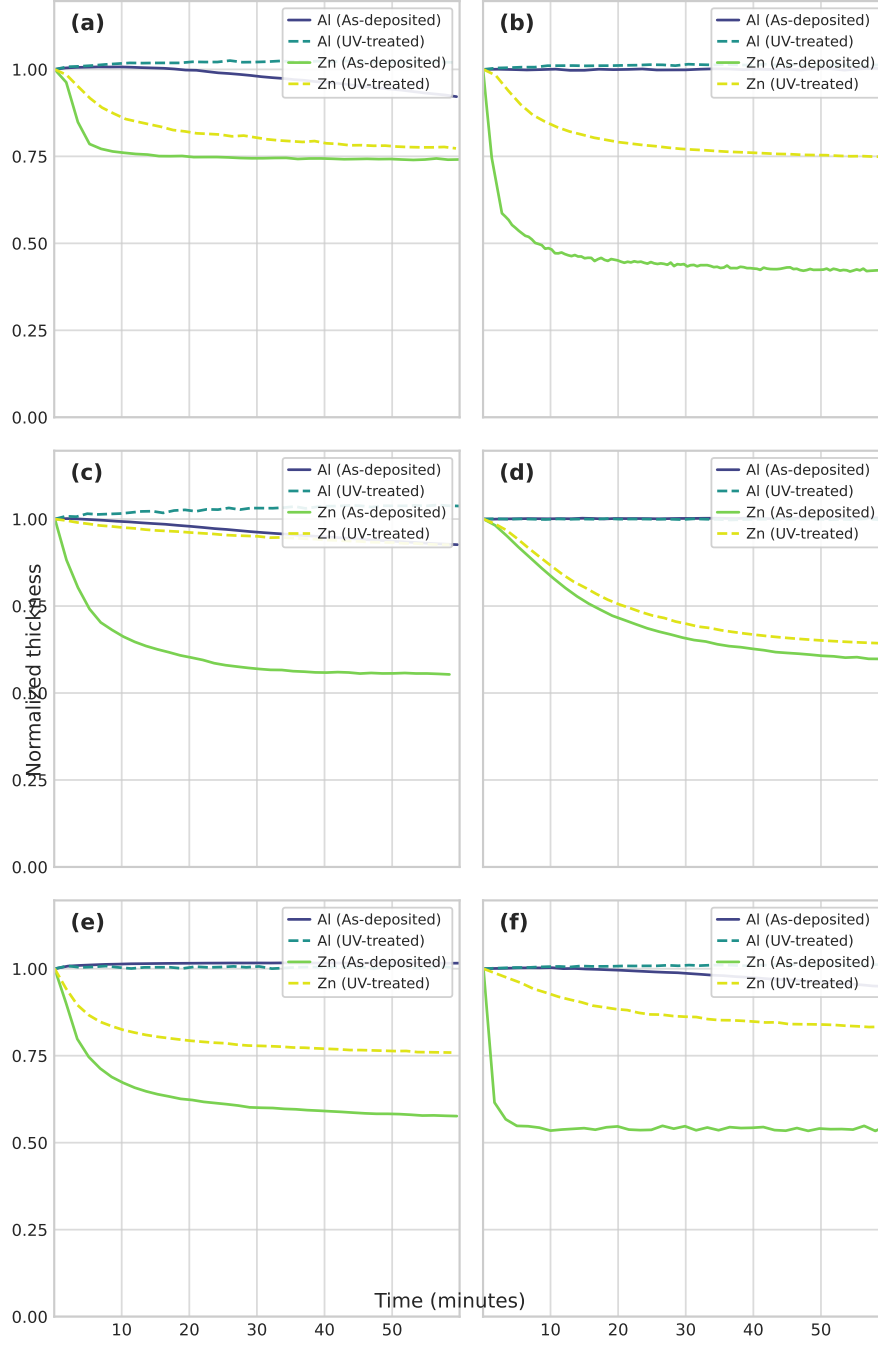
Figure 1: Normalized thickness change over 1 hour of air exposure for Al-based and Zn-based hybrid thin films incorporating different organic linkers. (a) MPD (methylenepropanediol); (b) EG (ethylene glycol); (c) THB (trihydroxybenzene); (d) BTY (1,4-butynediol); (e) DHB (dihydroxybutene); (f) CB (cis-butenediol). Solid lines represent as-deposited films, while dashed lines correspond to UV-treated films. Aluminum-based (Al) and zinc-based (Zn) films are distinguished by color. Thickness values were normalized to the initial thickness at time zero.

Developer Compatibility and Patterning Contrast

Chemical robustness was evaluated by immersing hybrid films in DI water, anhydrous organic solvents (acetone, toluene, chloroform), and dilute aqueous developers (0.01 M HCl and 0.01 M KOH) for 1 h. Post-treatment thicknesses and refractive indices were measured via spectroscopic ellipsometry.

Zincone films showed extreme sensitivity, rapidly dissolving in aqueous media and undergoing substantial degradation in organic solvents. This instability is consistent with the facile hydrolytic cleavage of Zn–O–C linkages upon exposure to moisture and polar solvents [26]. Although UV pretreatment provided modest improvements in handling stability, the inherent chemical fragility of zincones limited their viability for lithographic applications.

In contrast, alucone films displayed significantly greater chemical resistance. As-deposited alucones lost 10 % to 20 % thickness in DI water, indicative of partial hydrolysis. Organic solvents produced minor thickness increases and decreases in refractive index, likely due to limited solvent uptake and the formation of porous domains within the film [27]. UV-treated alucones retained both thickness and refractive index across all solvents and aqueous developers, reflecting their densified and crosslinked structure.

Three visualization formats were used to compare etch stability: (a) heatmaps of organic linker vs. solvent, (b) grouped bar charts with solvents on the x-axis and linkers grouped by color, and (c) grouped bar charts with linkers on the x-axis and solvents grouped by color. Organic linkers are ordered by chemical structure: EG (ethylene glycol), CB (cis-butenediol), BTY (butynediol), THB (trihydroxybenzene), MPD (methylenepropanediol), and DHB (dihydroxybutene). Solvents are ordered from aqueous (0.01 M HCl, 0.1 M KOH, water, ethanol) to polar aprotic (acetone) to nonpolar (chloroform, toluene). A consistent y-axis range was used to allow visual comparison between Al- and Zn-based films. Colors correspond to exposure condition using the Viridis colormap.

While both 0.01 M HCl and KOH fully removed the films with extended immersion, KOH was excluded from further development studies due to its aggressive etching of silicon substrates and risk of undercutting [28]. HCl enabled selective removal of unexposed regions via protonation and hydrolysis of metal–O–C bonds, making it the preferred developer.

Short-time immersion tests in 0.01 M HCl showed strong contrast between as-deposited and UV-treated alucones. UV treatment significantly delayed dissolution, enabling high-resolution patterning. This strong contrast informed the selection of alucone materials for subsequent electron-beam lithography (EBL) evaluation.
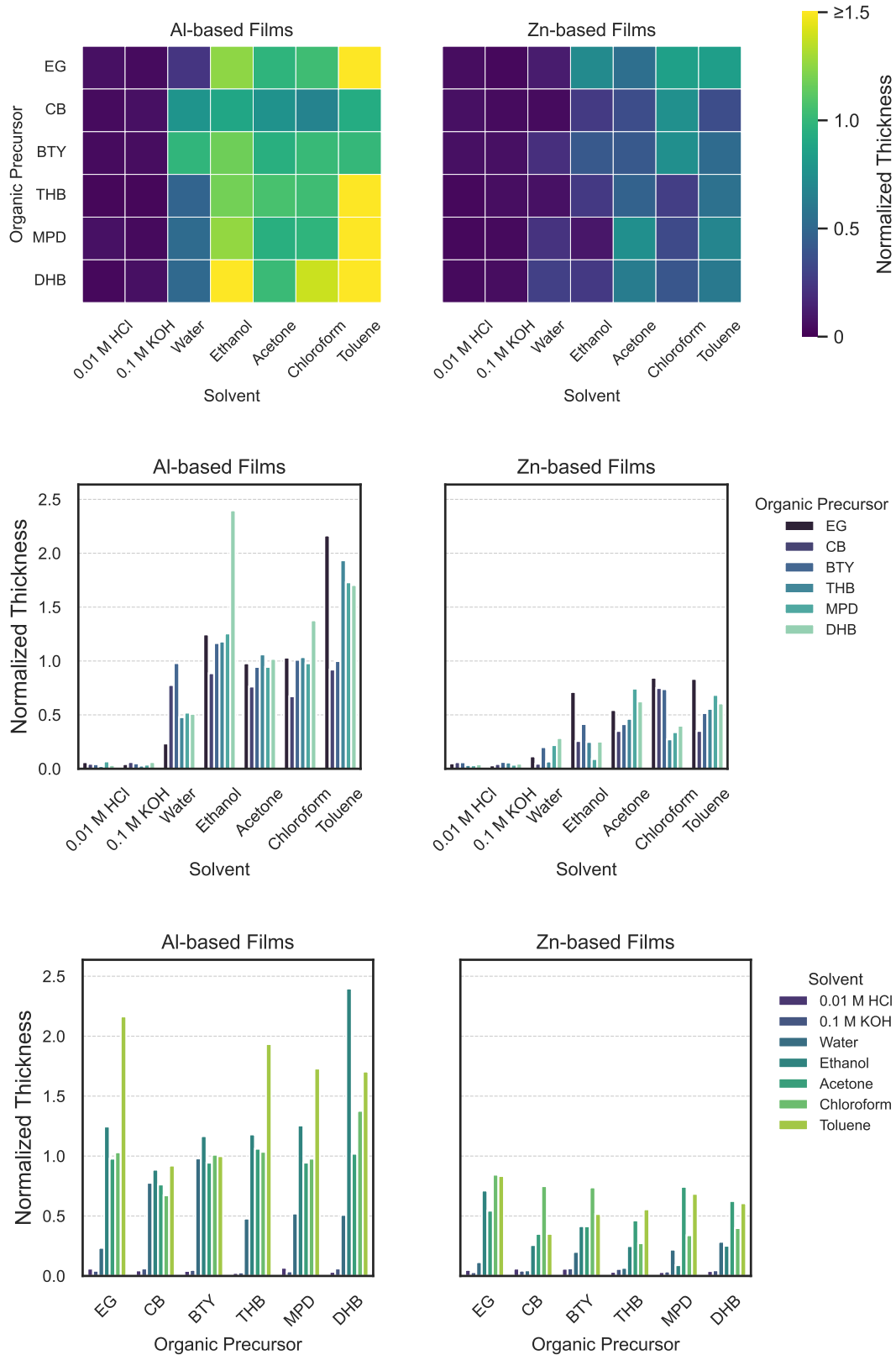
Figure 2: Normalized thickness of as-deposited hybrid films after 1 h solvent immersion, shown using three complementary visualization formats: **(a)** heatmaps of organic linker vs. solvent for Zn- and Al-based hybrid films (DEZ and TMA precursors, respectively); **(b)** grouped bar charts with solvents on the x-axis and organic linkers grouped by color; and **(c)** grouped bar charts with organic linkers on the x-axis and solvents grouped by color. Organic linkers are ordered by chemical structure: EG (ethylene glycol), CB (cis-butenediol), BTY (butynediol), THB (trihydroxybenzene), MPD (methylenepropanediol), and DHB (dihydroxybutene). Solvents are ordered from aqueous (0.01 M HCl, 0.1 M KOH, water, ethanol) to polar aprotic (acetone), and nonpolar (chloroform, toluene).

Selection of Lead Materials for Advanced Characterization

The results of air stability and chemical compatibility studies guided the selection of alucone films for further structural and spectroscopic characterization. The goal was to identify systems that not only exhibit UV-induced transformation but also demonstrate environmental robustness suitable for patterning applications.

Zincone films were excluded early due to their severe chemical instability under ambient and aqueous conditions. Their rapid hydrolysis, combined with concerns over zinc volatility and potential contamination under vacuum, made them unsuitable for further development [29].

Among the alucones, BTY-based films stood out for their high and consistent growth per cycle ($\sim$6 Å/cycle) and pronounced UV-induced chemical changes observed by both FTIR and XPS. These included the disappearance of hydroxyl features, emergence of conjugated C=C and C=O signals, and reduced susceptibility to hydrolysis, indicative of robust photochemical crosslinking. As a result, BTY was selected for detailed spectroscopic analysis and electron-beam lithography (EBL) evaluation.

THB-based alucones also exhibited good environmental stability, even without UV treatment. However, their FTIR and XPS spectra showed only subtle changes upon UV exposure, with limited evidence of crosslinking or significant structural reorganization. Due to this lack of responsiveness to UV activation, THB films were not advanced to lithographic testing. Still, their aromaticity and partial degradation resistance justified their inclusion as a chemically stable control for extended spectroscopic analysis.

Other organic linkers, such as CB and MPD, were deprioritized. CB-based films showed moderate UV-induced stabilization but fell short of the crosslinking efficiency observed in BTY. MPD-based films exhibited minimal chemical change with UV exposure and poor aqueous stability, indicating limited suitability for further development.

In summary, BTY and THB alucones were selected as lead candidates for advanced FTIR and XPS characterization. BTY-based films were prioritized for lithography due to their strong UV response and structural transformation, while THB-based films served as a stable aromatic control to explore the boundaries of UV-induced network modification.

FTIR Analysis: UV-Induced Crosslinking and Network Densification

Fourier-transform infrared (FTIR) spectroscopy was used to analyze the chemical and structural changes induced by ultraviolet (UV) exposure (254 nm) in TMA–BTY alucone films. Spectra acquired before and after UV irradiation revealed clear modifications in vibrational modes associated with hydroxyl, carbon–carbon, and metal–oxygen bonding environments, providing mechanistic insight into crosslinking and network densification (Figure 3).

As-deposited films showed broad O–H stretching bands centered near 3622 and 3232 1/cm, corresponding to free and hydrogen-bonded hydroxyl groups, respectively. These bands were significantly diminished after UV exposure, indicating consumption of terminal –OH groups via condensation, elimination, or photochemical reactions. This is consistent with the disappearance of hydroxyl signatures in post-UV XPS and supports a densification mechanism driven by hydroxyl removal.

A key transformation was the emergence and sharpening of the band at 1612/cm, attributed to C=C stretching vibrations. This suggests the formation of conjugated or aromatic domains, likely resulting from cycloaddition or radical-mediated rearrangement of BTY's internal alkyne units. Although C C stretching modes were obscured by overlapping CO_2 features, the evolution of C=C peaks provides indirect evidence of alkyne conversion.

In the fingerprint region, characteristic Al–O–C backbone vibrations appeared between 1200/cm to 800/cm, including strong peaks at 1132, 1063, and 1012 1/cm, along with broader modes below 700 1/cm. Following UV exposure, these bands narrowed and sharpened, consistent with increased structural order. Al–O bending vibrations near 579 and 557 1/cm also became more defined, indicating enhanced crosslink density.

Collectively, these spectral changes support a mechanism where UV irradiation removes hydroxyl groups, induces alkyne–alkyne or alkyne–hydroxyl coupling, and promotes rearrangement into conjugated or partially aromatic structures. These transformations reduce free volume, increase cohesion, and improve resistance to hydrolysis—consistent with the enhanced film stability observed in chemical and aqueous testing.
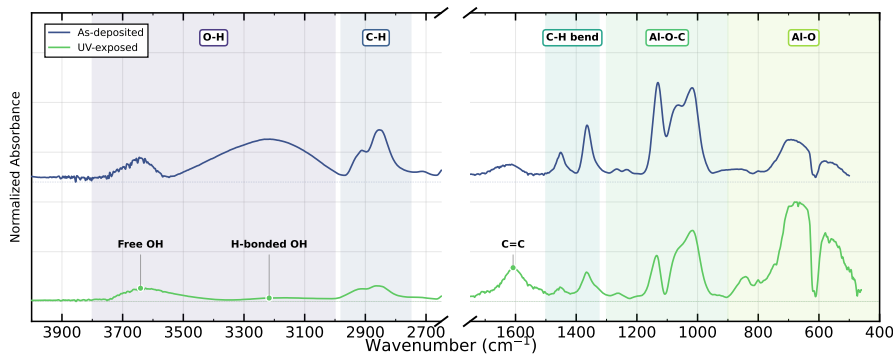
Figure 3: FTIR spectra of TMA–BTY alucone films before and after UV irradiation at 254 nm. Notable changes include disappearance of O–H stretching bands (3622 and 3232 1/cm), emergence of a sharp C=C stretch near 1612 1/cm, and sharpening of Al–O–C and Al–O bending modes in the fingerprint region. These features are consistent with UV-induced crosslinking and structural densification.

XPS Analysis of Bonding Environments and Stability

X-ray photoelectron spectroscopy (XPS) was used to investigate chemical bonding environments and UV-induced structural transformations in alucone films. High-resolution spectra of the C 1s, O 1s, and Al 2p regions were collected for both BTY- and THB-based films across three conditions: as-deposited, water-exposed, and UV+water-exposed.

BTY-Based Films (TMA–BTY)

In the Al 2p region, all BTY samples showed a primary peak near 74.6 eV, consistent with Al–O–C linkages. The as-deposited film exhibited a symmetric profile, while the water-exposed sample developed a low-binding-energy shoulder, attributed to Al–OH or Al–O–Al formation through hydrolysis. The UV+water-treated film retained a symmetric peak with minimal shoulder, indicating UV pretreatment effectively suppressed hydrolytic transformation.

O 1s spectra showed a dominant peak near 532 eV assigned to Al–O–C environments, with minor higher-binding-energy features from hydroxyls. Water exposure broadened and shifted the peak, indicating increased hydroxyl content and framework disruption. In contrast, the UV+water sample preserved a narrower, more symmetric envelope, consistent with structural retention and reduced hydrolysis.

C 1s spectra in as-deposited BTY films revealed primary components corresponding to aliphatic C–C/C–H, C–O, and minor oxidized species. A very subtle low-binding-energy shoulder was observed near 283 eV, possibly arising from Al–C bonds in residual

unreacted TMA ligands. This feature was not included in peak fitting due to its low intensity but may indicate trace surface-bound methyl groups.

Upon water exposure, the C–C and C–O components were attenuated, and C=O and carbonate peaks intensified, indicating degradation of the organic matrix. In contrast, UV+water-treated films retained more C–C and C–O character but also showed a pronounced increase in the C=O contribution. This suggests that UV exposure drives bond scission and rearrangement—possibly involving C–O cleavage and formation of conjugated or aromatic carbonyl structures. These changes support a transition to a chemically stabilized, denser framework—further explored in the next section.

Quantitative analysis (Table 1) supports this interpretation. Water exposure increased oxygen content from 29.2% to 56.0% and decreased carbon from 58.9% to 18.6%, consistent with hydrolysis and organic loss. UV pre-treatment reduced this effect: the UV+water sample retained 55.6% carbon and 32.9% oxygen, with aluminum content closer to the as-deposited state.

THB-Based Films (TMA–THB)

THB-based films exhibited Al–O–C peaks in the Al 2p region near 74.6 eV. The water-exposed sample developed a low-binding-energy shoulder (Al–OH/Al–O–Al), while the UV+water spectrum maintained a narrower, symmetric peak, suggesting partial protection of the coordination environment.

O 1s spectra showed similar trends: the as-deposited film exhibited a peak near 532.0 eV, while water exposure caused broadening and the appearance of a low-binding-energy shoulder (530.8 eV). The UV+water spectrum remained close to the as-deposited profile.

C 1s spectra for THB films included aromatic C–C, C–O, and minor oxidized features. A faint shoulder near 283 eV, possibly corresponding to Al–C bonding from trace unreacted TMA, was observed but not fitted. Water exposure reduced overall carbon signal and increased oxidized species. UV-treated samples retained more C–O content and exhibited less oxidation, indicating protection of the aromatic linker. However, the changes were less pronounced than in BTY, consistent with THB's inherent chemical stability and a more limited UV-induced structural transformation.
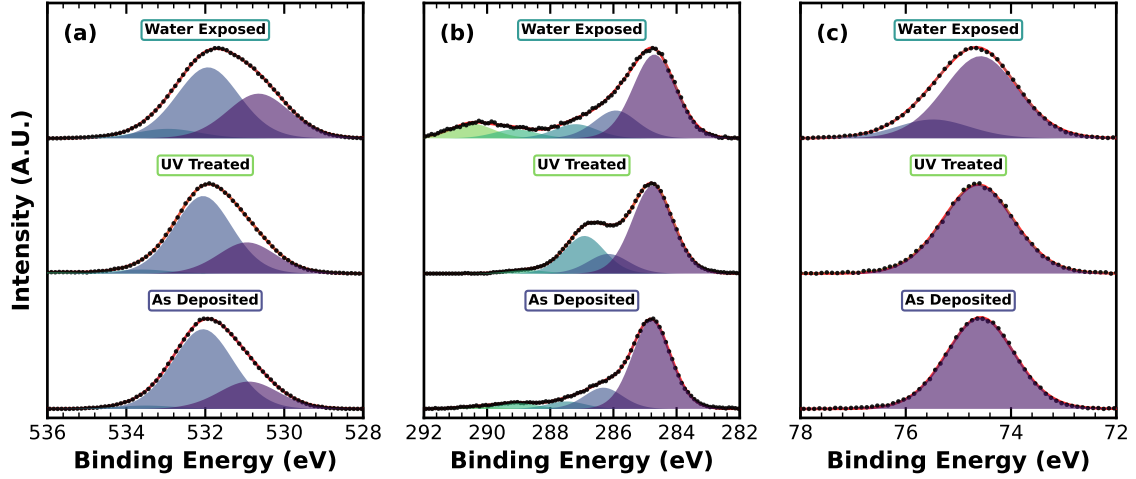
Figure 4: High-resolution XPS spectra of BTY-based alucone films across as-deposited, water-exposed, and UV+water-exposed conditions. Columns show C 1s (left), O 1s (middle), and Al 2p (right) regions. Colored lines denote individual fit components; black crosses represent measured data.

> **Placeholder: THB XPS Spectra**
> High-resolution XPS for THB-based alucone films
> (C 1s, O 1s, Al 2p regions)

Figure 5: High-resolution XPS spectra of THB-based alucone films across as-deposited, water-exposed, and UV+water-exposed conditions. Columns show C 1s (left), O 1s (middle), and Al 2p (right) regions. Colored lines denote individual fit components; black crosses represent measured data.

Table 1: Renormalized atomic % (mean ± standard deviation) for O, C, and Al in TMA–BTY and TMA–THB alucone films across treatments. Ideal MLD values are calculated based on precursor stoichiometry.

Treatment	BTY [%]			THB [%]		
	O	C	Al	O	C	Al
As-Deposited	29.2 ± 0.8	58.9 ± 0.4	11.9 ± 0.5	42.8 ± 1.8	25.9 ± 2.4	31.3 ± 0.6
H$_2$O-Exposed	56.0 ± 0.5	18.6 ± 0.5	25.3 ± 0.3	50.2 ± 0.6	17.2 ± 1.6	32.6 ± 1.0
H$_2$O + UV	32.9 ± 1.2	55.6 ± 1.5	11.5 ± 0.4	46.8 ± 1.0	20.2 ± 1.2	33.0 ± 0.1
Ideal (MLD)	20.0	70.0	10.0	23.1	69.2	7.7

Mechanistic Insight into UV-Induced Stabilization

The combined spectroscopic evidence from FTIR and XPS supports a mechanistic model for UV-induced stabilization in TMA–BTY alucone films. Figure 6 schematically illustrates the proposed evolution from the as-deposited structure to a UV-crosslinked and chemically stabilized network.

As-deposited alucone films consist of alternating Al–O– and organic segments formed from trimethylaluminum (TMA) and 1,4-butynediol (BTY), with a backbone structure nominally described as $[-Al-O-CH_2-C{\equiv}C-CH_2-O-]$. FTIR analysis reveals residual hydroxyl bands near 3622 and 3232 1/cm, indicating incomplete surface reactions or unreacted diol end-groups. XPS data further suggests a small population of methyl species (Al–C) likely originating from unreacted TMA ligands at the surface.

Upon UV exposure at 254 nm, substantial chemical transformations occur. FTIR shows strong attenuation of O–H bands and the emergence of a sharp peak at 1612/cm, indicative of conjugated C=C species. Concurrently, XPS reveals a significant increase in C=O contributions alongside a reduction in C–O intensity, implying cleavage of C–O bonds and oxidative rearrangement.

We propose that these spectral changes reflect a multi-step transformation initiated by UV-induced radical or [2+2] cycloaddition reactions between adjacent alkyne moieties. These reactions generate conjugated or aromatic domains and disrupt the original ether-like linkages. The newly formed C=O species likely arise from oxidation of alkyne-adjacent carbons, forming carbonyl-containing structures reminiscent of quinones. These conjugated C=C and C=O groups contribute to electron delocalization, stabilizing the hybrid network through aromatic or quasi-aromatic resonance.

This photochemical crosslinking is further supported by sharpening of fingerprint-region FTIR bands and retention of Al–O–C character in Al 2p and O 1s XPS spectra. The resulting structure is chemically denser, less permeable to water, and resistant to hydrolysis. By contrast, non-irradiated films show pronounced degradation under aqueous exposure, with loss of carbon and formation of hydrolyzed Al–O–Al species.

While THB-based alucone films also showed modest UV-induced stabilization and good intrinsic resistance to hydrolysis, their spectroscopic profiles revealed only subtle changes upon irradiation, with minimal evidence of crosslinking or new conjugated features. The absence of significant C=O growth or structural reorganization suggests

limited potential for negative-tone resist behavior, where crosslinking and developer resistance are essential. Consequently, BTY-based alucones were selected as the lead candidate for electron-beam lithography evaluation, owing to their pronounced photochemical reactivity and structural transformation upon UV exposure.

> **Placeholder: Structure Evolution Figure**
> Schematic showing proposed UV-induced crosslinking mechanism

Figure 6: Proposed structural evolution and chemical transformations of BTY-based alucone films during UV irradiation and subsequent hydrolytic exposure: (a) as-deposited film containing residual hydroxyl groups and isolated alkyne linkages, (b) UV-treated film exhibiting crosslinked conjugated structures and reduced hydroxyl content, and (c) hydrolytically degraded film without UV treatment, illustrating extensive bond cleavage and porous structure formation.

Electron-Beam Lithography Studies

The lithographic performance of BTY-based alucone films was evaluated using electron-beam lithography (EBL) on a JEOL JBX-6300FS system operating at $100\,\text{kV}$. Films were flood-exposed to UV light prior to EBL to initiate partial crosslinking, as established in previous sections.

A dose matrix was patterned onto the films and developed in $0.01\,\text{M}$ HCl for $10\,\text{s}$. Well-defined square features were observed across a dose range of $500\,\mu\text{C/cm}^2$ to $2000\,\mu\text{C/cm}^2$. Above $2000\,\mu\text{C/cm}^2$, haloing effects became apparent at feature boundaries, attributed to electron scattering and proximity effects, resulting in excess material retention beyond the intended dose region.

Profilometry measurements were performed across individual squares to quantify retained film thickness as a function of dose. These data confirmed a negative-tone resist response, with increasing thickness corresponding to increasing dose up to saturation. Step height measurements will be used to extract contrast and dose-to-clear values (Figure 7).

Atomic force microscopy (AFM) was used to characterize the edges and corners of squares within the optimal dose range. These scans revealed sharp edge definition, minimal roughness, and flat residual film topography, consistent with clean pattern transfer and uniform development. Representative AFM images and surface height profiles are shown in Figure 8. Full surface maps and extended profiles are included in the Supple-

mentary Information.

A second pattern consisting of box and grating features was exposed using the optimal dose identified from the matrix. Scanning electron microscopy (SEM) and AFM imaging of these features are being used to evaluate resolution, line edge roughness (LER), and three-dimensional profile fidelity. Together, these measurements establish BTY-based alucone as a negative-tone hybrid resist with robust developer contrast, submicron pattern resolution, and compatibility with acidic development.

Figure 7: Dose matrix layout and representative square features used to evaluate lithographic contrast in BTY-based alucone films. Step height data across each square was used to generate a contrast curve. Final figure will include profilometry overlay.
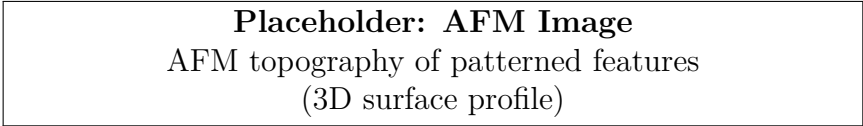

Placeholder: AFM Image
AFM topography of patterned features
(3D surface profile)

Figure 8: AFM image of the corner of a BTY-based alucone square developed after EBL exposure at the optimal dose. Sharp corner retention and flat film interior indicate effective negative-tone patterning. Surface map and line profile shown.

3.8.1   SEM

SEM imaging was carried out on the dose matrix consisting of 100 µm × 100 µm square patterns with doses ranging from 100 to 30,000 µC/cm². Additionally, fine feature ma-

trices were imaged to assess resolution capabilities.

3.8.2   Dose Matrices and Contrast Curve Analysis

Contrast curves were generated from both SEM and AFM measurements to characterize the resist response across different developers. The normalized thickness data revealed distinct crosslinking and graphitization regions, necessitating a segmented fitting approach.

For the crosslinking region (low to moderate doses), a sigmoid function was fitted:

$$f(D) = \frac{1}{1 + (D_{50}/D)^\gamma} \tag{1}$$

where D_{50} is the dose at 50% normalized thickness and γ is the contrast parameter.

For the graphitization region (high doses), a linear decay function was applied:

$$f(D) = \text{slope} \times D + \text{intercept} \tag{2}$$

The AFM measurements on 2 µm line gratings (1 µm gap) showed similar behavior, with thickness increasing to a peak followed by reduction at high doses. The average contrast across all developers was $\gamma = 2.54$, with individual values of:

- 0.005M HCl 10s: $\gamma = 0.91$, $D_{50} = 1225.1$ µC/cm²

- 0.01M HCl 10s: $\gamma = 3.25$, $D_{50} = 9223.7$ µC/cm²

- 0.01M HCl 5s: $\gamma = 3.44$, $D_{50} = 2447.5$ µC/cm²

Notably, the two 0.01M developers exhibited similar high contrast values ($\gamma \approx 3.3 - 3.4$), as expected for identical developer concentrations, while the 0.005M developer showed significantly lower contrast ($\gamma = 0.91$). The 0.01M HCl 10s sample showed no thickness reduction even at the highest doses (30,000 µC/cm²), suggesting incomplete graphitization under these development conditions. In contrast, both the 0.005M 10s and 0.01M 5s samples exhibited clear decay regions above their respective peak doses (3000 and 7000 µC/cm²).

The SEM-based contrast curve (Figure X) showed good agreement with the AFM data, with a clear transition at approximately 3958 µC/cm² between the crosslinking

and graphitization regions. The normalized SEM gray values demonstrated the expected sigmoid behavior in the crosslinking region, transitioning to exponential decay at high doses as the resist underwent densification and carbonization.

Conclusion

In this study, we systematically explored the growth, stability, chemical transformations, and lithographic performance of hybrid organic–inorganic films deposited via molecular layer deposition (MLD), focusing specifically on alucone and zincone networks formed with a range of bifunctional organic diols. Comprehensive evaluation of film deposition, environmental stability, chemical robustness, and developer compatibility identified alucone films based on 1,4-butynediol (BTY) and trihydroxybenzene (THB) as the most promising candidates for advanced lithographic applications.

Key findings include the critical role of UV-induced crosslinking in substantially enhancing the stability and chemical resistance of alucone networks. FTIR spectroscopy demonstrated clear evidence of photochemically initiated crosslinking reactions, resulting in increased network densification, reduction of residual hydroxyl groups, and enhanced conjugation within the hybrid structure. Complementary XPS analyses confirmed that UV-induced crosslinking effectively stabilizes Al–O–C linkages, substantially inhibiting hydrolytic degradation and preserving the organic framework integrity upon exposure to aqueous environments.

Developer compatibility tests established that dilute hydrochloric acid provides excellent chemical contrast between UV-treated and as-deposited alucone films, making it an ideal choice for subsequent lithographic development processes. Electron-beam lithography (EBL) studies further revealed significant improvements in sensitivity, resolution, and contrast for UV-stabilized alucones. Specifically, UV-treated BTY-based alucone films exhibited exceptional negative-tone lithographic behavior, enabling reproducible sub-50 nm feature patterning at substantially reduced electron-beam doses compared to conventional inorganic resist systems.

The detailed mechanistic insights obtained from combined FTIR and XPS analyses established that UV-induced organic crosslinking is the primary driver behind the observed stabilization and lithographic performance improvements. Unlike previously studied alu-

cone systems relying solely on inorganic densification, the organic crosslinking approach demonstrated here provides superior sensitivity, pattern fidelity, and overall lithographic performance.

Collectively, these results highlight the substantial potential of UV-stabilized alucone films as advanced hybrid resists for high-resolution, low-dose electron-beam lithography and possibly extreme ultraviolet (EUV) lithography applications. The clear relationship between chemical composition, UV-induced network densification, environmental robustness, and lithographic performance demonstrated in this work provides valuable guidelines for designing next-generation hybrid materials tailored specifically for advanced nanoscale patterning technologies.

Acknowledgements

Author Contributions

D.R. performed all experiments and analysis. All authors contributed to manuscript preparation.

Conflicts of Interest

The authors declare no conflicts of interest.

Data Availability Statement

All data supporting the findings of this study are available from the corresponding author upon reasonable request.

References

1. Zhang, G., Moreau, W. M. & Wagner, R. S. Sensitivity Enhancement of Chemically Amplified Resists and Performance Study Using Extreme Ultraviolet Interference Lithography. *Journal of Micro/Nanolithography, MEMS, and MOEMS* **15,** 033502 (2016).

2. Xu, H., Kosma, V., Giannelis, E., Ober, C. K. & Sakai, K. *EUV Photolithography: Resist Progress and Challenges* in *Extreme Ultraviolet (EUV) Lithography IX* **10583** (SPIE, 2018), 1058306.

3. Manouras, T. & Argitis, P. High-Sensitivity Resists for EUV Lithography: A Review of Material Design Strategies and Performance Results. *Nanomaterials* **10,** 1593 (2020).

4. Mojarad, N., Gobrecht, J. & Ekinci, Y. Beyond EUV Lithography: A Comparative Study of Efficient Photoresists' Performance. *Scientific Reports* **5,** 9235 (2015).

5. Vesters, Y. *et al. Unraveling the Role of Photons and Electrons upon Their Chemical Interaction with Photoresist during EUV Exposure* in *Extreme Ultraviolet (EUV) Lithography IX* **10586** (SPIE, 2018), 105860C.

6. Harumoto, T., Yamamoto, Y. & Nishimura, N. Sensitivity and line edge roughness of chemically amplified resists for EUV lithography: Analysis and trade-offs. *Journal of Photopolymer Science and Technology* **34,** 239–246 (2021).

7. Cardineau, B. e. a. *EUV Resists Based on Tin-Oxo Clusters* in *Photomask Technology 2014* **9235** (SPIE, 2014), 923509.

8. Saifullah, M. S. M., Tiwale, N. & Ganesan, R. Metal-Containing Resists in Electron-Beam Lithography: Perspectives for Extreme Ultraviolet Patterning. *Journal of Micro/Nanopatterning, Materials, and Metrology* **21,** 041402 (2022).

9. Ravi, A., Shi, J., Lewis, J. & Bent, S. F. *Molecular Layer Deposition of an Al-Based Hybrid Resist for Electron-Beam and EUV Lithography* in *Advances in Patterning Materials and Processes XL* **12498** (SPIE, 2023), 1249802.

10. Shi, J., Ravi, A., Richey, N. E., Gong, H. & Bent, S. F. Molecular Layer Deposition of a Hafnium-Based Hybrid Thin Film as an Electron-Beam Resist. *ACS Applied Materials & Interfaces* **14,** 27140–27148 (2022).

11. Marichy, C., Bechelany, M. & Pinna, N. Atomic Layer Deposition of Nanostructured Materials for Energy and Environmental Applications. *Advanced Materials* **24,** 1017–1032 (2012).

12. Meng, X. An Overview of Molecular Layer Deposition for Organic and Organic–Inorganic Hybrid Materials: Mechanisms, Growth Characteristics, and Promising Applications. *Journal of Materials Chemistry A* **5,** 18326–18378 (2017).

13. Multia, J. & Karppinen, M. Atomic/Molecular Layer Deposition for Designer's Functional Metal–Organic Materials. *Advanced Materials Interfaces* **9,** 2200210 (2022).

14. Vemuri, R. K. & George, S. M. Molecular Layer Deposition of Hybrid Organic–Inorganic Films: Recent Advances and Applications. *Journal of Vacuum Science Technology A* **41,** 040801 (2023).

15. Lee, B., Heo, J.-S., Lee, J. & Lee, B. Atomic Layer Deposition of Alucone Organic–Inorganic Hybrid Films Using Trimethylaluminum and Ethylene Glycol. *The Journal of Physical Chemistry C* **115,** 16862–16868 (2011).

16. Weckman, T. & Laasonen, K. Atomic Layer Deposition of Zinc Oxide: Diethyl Zinc Reactions and Surface Saturation from First-Principles. *The Journal of Physical Chemistry C* **120,** 21460–21471 (2016).

17. Choudhury, D., Rajaraman, G. & Sarkar, S. K. Stability of Molecular Layer Deposited Zincone Films: Experimental and Theoretical Exploration. *RSC Advances* **5,** 29947–29952 (2015).

18. Perrotta, A., Berger, R., Muralter, F. & Coclite, A. M. Mesoporous ZnO Thin Films Obtained from Molecular Layer Deposited "Zincones". *Dalton Transactions* **48,** 14178–14188 (2019).

19. Lee, B. H., Anderson, V. R. & George, S. M. Growth and Properties of Hafnicone and HfO_2/Hafnicone Nanolaminate and Alloy Films Using Molecular Layer Deposition Techniques. *ACS Applied Materials & Interfaces* **6,** 16880–16887 (2014).

20. Choe, Y., Reece, D. & Bergsman, D. S. High-Throughput Multiplexing Reactor Design for Rapid Screening of Atomic/Molecular Layer Deposition Processes. *Journal of Vacuum Science & Technology A* **42** (2024).

21. Wang, Y., Zhang, X. & Liu, J. Atomic/molecular layer deposition mechanism of alucone organic–inorganic hybrid films. *Materials Today Communications* **33,** 103634 (2022).

22. Smith, A., Johnson, B. & Lee, C. Thickness of molecular layer deposited zincone and percentage of the remaining ZnO after aging. *Thin Solid Films* **765,** 139123 (2023).

23. Zhao, L., Chen, M. & Wang, Y. Crosslinking-induced patterning of MOFs by direct photo and electron beam lithography. *Nature Communications* **14,** 40590 (2023).

24. Nguyen, T., Kim, H. & Lee, J. High-resolution chemical patterns from negative tone resists for the fabrication of nanoscale devices. *Journal of Vacuum Science Technology B* **41,** 023007 (2023).

25. Park, S., Choi, D. & Kim, Y. Ultralow line edge roughness of hybrid multilayer extreme ultraviolet resists. *Materials Today* **50,** 45–52 (2025).

26. King, D. M., Liang, X., Weimer, A. W. & George, S. M. Atomic layer deposition of organic-inorganic hybrid materials based on rigid aromatic molecules. *Chemistry of Materials* **21,** 3307–3316 (2009).

27. Vemuri, R. K., Solterbeck, C. H. & George, S. M. Molecular Layer Deposition of Hybrid Organic–Inorganic Films Using Trimethylaluminum and Ethylene Glycol. *Journal of Vacuum Science Technology A* **26,** 544–557 (2008).

28. Horie, K., Mita, I. & Kambe, H. *Photochemistry of Polymer Materials: Fundamentals and Applications* (Springer, 2010).

29. Richey, N. E. & Bent, S. F. Nucleophilic Degradation Pathways in Hybrid Thin Films: Mechanisms and Kinetics. *Chemistry of Materials* **31,** 6042–6050 (2019).

Table S1: Optimized molecular layer deposition parameters for each organic precursor.

Organic Precursor	Chamber Temp. (°C)	Organic Temp. (°C)	N₂ Overlap (s)	Pump Overlap (s)	Dose (s)	Purge (s)
Ethane-1,2-diol (EG)	120	[EG Temp.]	[N₂ overlap]	[Pump overlap]	[Dose]	300
cis-2-Butene-1,4-diol (CB)	120	[CB Temp.]	[N₂ overlap]	[Pump overlap]	[Dose]	300
2-Methylene-1,3-propanediol (MPD)	120	[MPD Temp.]	[N₂ overlap]	[Pump overlap]	[Dose]	300
1,3,4-Trihydroxybenzene (THB)	120	65	[N₂ overlap]	[Pump overlap]	[Dose]	300
1,4-Butynediol (BTY)	120	60	[N₂ overlap]	[Pump overlap]	[Dose]	300
3,4-Dihydroxy-1-butene (DHB)	120	[DHB Temp.]	[N₂ overlap]	[Pump overlap]	[Dose]	300

Supplementary Information

Table S1: Organic Precursor Deposition Parameters

Note: Precise values of N_2 overlap, pump overlap, and organic precursor doses were optimized individually based on precursor volatility and deposition performance.

Table S2: Typical MLD Cycle Sequence Parameters

Table S2: General sequence parameters used in molecular layer deposition cycles.

Step	Temperature (°C)	Pressure (mTorr)	Duration (s)
N_2 purge	120	200	300
TMA/DEZ dose	120	200	$[t_{inorg}]$
N_2 overlap	120	200	$[t_{overlap}]$
Pump down	120	50	$[t_{pump}]$
Organic dose	120	200	$[t_{org}]$
Shared purge	120	200	300

Notes: Durations for organic and inorganic precursor dosing steps were adjusted based on precursor-specific requirements.

Table S3: Peak positions and relative areas for O 1s XPS spectra across bonding environments.

Sample	Al–O–Al (Lattice O)		Al–O–C (Hydroxyl O)		Adsorbed/Oxidized O	
	Peak Position (eV)	% Area	Peak Position (eV)	% Area	Peak Position (eV)	% Area
As Deposited	530.9	27.7	532.0	68.8	533.5	3.5
Water Exposed	530.7	36.1	532.0	57.3	533.1	6.6
Water Exposed UV	531.0	24.8	532.1	72.4	533.9	2.9

Table S4: Peak positions and relative areas for C 1s XPS spectra across bonding environments.

Sample	C–C/C–H (fit1)		C–O (fit2)		C=O (fit3)		Carbonate/Oxidized (fit4)		Highly Oxidized (fit5)	
	Peak (eV)	% Area	Peak (eV)	% Area	Peak (eV)	% Area	Peak (eV)	% Area	Peak (eV)	% Area
As Deposited	284.8	61.6	286.7	35.0	288.6	3.4	–	–	–	–
Water Exposed	284.8	55.9	286.1	18.3	287.4	9.2	289.3	7.0	290.6	9.7
Water Exposed UV	284.9	68.8	286.4	17.2	287.6	6.4	289.1	5.2	290.5	2.3

Table S5: Peak positions and relative areas for Al 2p XPS spectra across bonding environments.

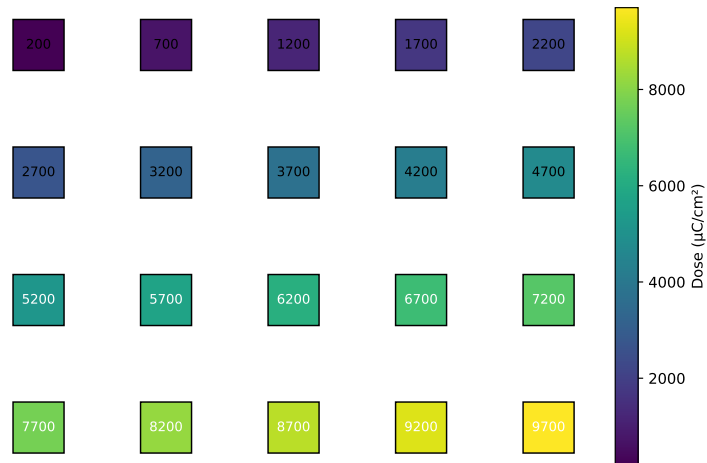| Sample	Primary Al (fit1)		Oxidized/Hydrolyzed Al (fit2)	
	Peak Position (eV)	% Area	Peak Position (eV)	% Area
As Deposited	74.6	100.0	–	–
Water Exposed	74.6	81.9	75.5	18.1
Water Exposed UV	74.6	100.0	–	–

Figure S1: Mockup of the electron beam lithography dose matrix. Each square represents a dose from 200 to 9700 μC/cm^2, color-coded for visualization.
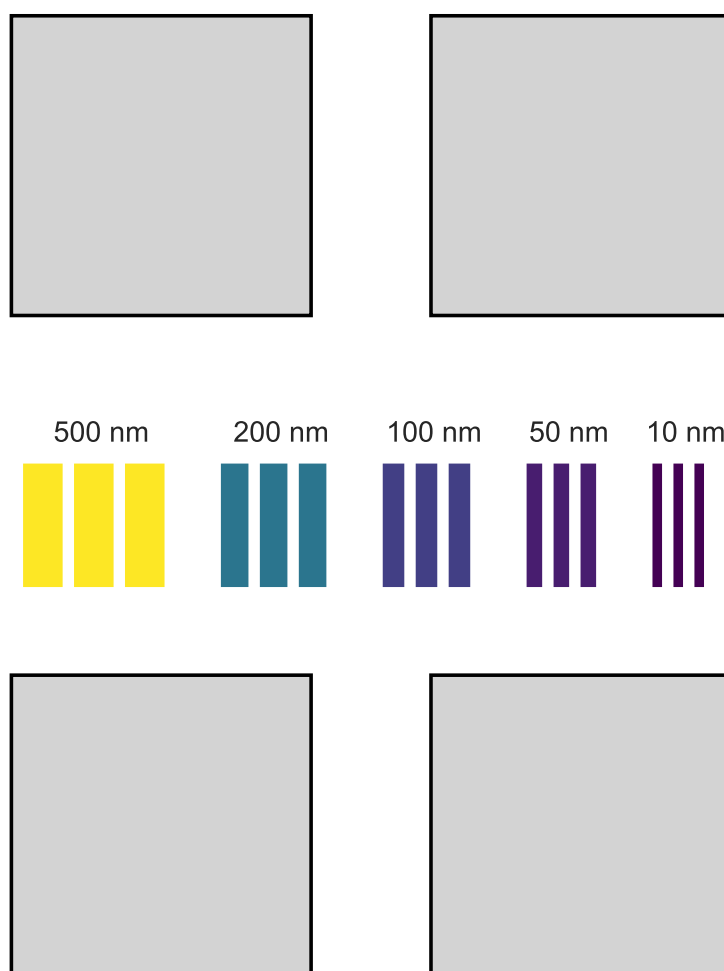

Figure S2: Mockup of four resist test regions surrounding a centered line-space grating array. Each grating group contains three lines of fixed visual width representing target linewidths from 500 nm to 10 nm. Grating bars are color-coded using the Viridis colormap to aid visual differentiation. This layout replicates the spatial structure of GDS files used for resolution and exposure testing.

Randomization and Control Scripts

Substrate randomization and reactor scheduling scripts are available at: https://github.com/BergsmanGroup/MLD_high_throughput